

## Tilting during island growth of $\text{In}_2\text{O}_3$ on Y-stabilized $\text{ZrO}_2(001)$ revealed by high-resolution x-ray diffraction

R. A. Cowley,<sup>1,2</sup> A. Bourlange,<sup>3</sup> J. L. Hutchison,<sup>4</sup> K. H. L. Zhang,<sup>3</sup> A. M. Korsunsky,<sup>5</sup> and R. G. Egdell<sup>3</sup>

<sup>1</sup>Clarendon Laboratory, Department of Physics, University of Oxford, Parks Road, Oxford OX1 3PU, United Kingdom

<sup>2</sup>Diamond Light Source Limited, Rutherford Appleton Laboratory, Didcot, Oxfordshire OX11 0QX, United Kingdom

<sup>3</sup>Department of Chemistry, Chemistry Research Laboratory, University of Oxford, Mansfield Road, Oxford OX1 3TA, United Kingdom

<sup>4</sup>Department of Materials, University of Oxford, Parks Road, Oxford OX1 3PH, United Kingdom

<sup>5</sup>Department of Engineering Science, University of Oxford, Parks Road, Oxford OX1 3PJ, United Kingdom

(Received 19 May 2010; revised manuscript received 13 August 2010; published 8 October 2010)

The growth of  $\text{In}_2\text{O}_3$  islands on (001)-oriented Y-stabilized cubic  $\text{ZrO}_2$  has been investigated using high-resolution x-ray diffraction and the results compared with those from atomic force microscopy and electron microscopy. Measurements were performed with wave-vector transfer both parallel to and perpendicular to the surface normal. Transverse scans around the epilayer (004) and (008) reflections gave a characteristic three-peak structure for wave-vector transfer along the [110] direction but a two-peak structure when the scan was performed along the [100] direction. These results suggest that the atomic planes of the islands are not parallel to those of the substrate but are tilted at an angle of about  $0.7^\circ$  from the four different in-plane  $\langle 110 \rangle$  directions. Tilting was also observed in real space by high-resolution transmission electron microscopy. The tilt helps to relieve tensile strain arising from a  $-1.6\%$  lattice mismatch between the epilayer and the substrate. The tilt direction is shown to be determined by the elastic constants of the epilayer, which favor strain along  $\langle 110 \rangle$  directions rather than  $\langle 100 \rangle$  directions. The x-ray results also indicated that the islands imaged by atomic force microscopy are each built up from microdomains so that the coherence length deduced from x-ray scattering is much smaller than the island size. Thus for islands with a thickness of  $2500 \text{ \AA}$  the coherence length was estimated to be about  $500 \text{ \AA}$ .

DOI: [10.1103/PhysRevB.82.165312](https://doi.org/10.1103/PhysRevB.82.165312)

PACS number(s): 68.55.ag, 68.35.bg, 81.10.Pq

### I. INTRODUCTION

In common with many other sesquioxide including  $\text{Mn}_2\text{O}_3$  and rare-earth oxides from  $\text{La}_2\text{O}_3$  to  $\text{Lu}_2\text{O}_3$ , indium oxide ( $\text{In}_2\text{O}_3$ ) adopts the cubic bixbyite structure. The crystal structure is based on a slightly distorted face-centered-cubic array of indium cations with  $\frac{3}{4}$  of the tetrahedral sites occupied by oxygen ions. The unit cell is body centered and belongs to the space group  $Ia\bar{3}$ . The structure can alternatively be described as a  $2 \times 2 \times 2$  superstructure of fluorite but with  $\frac{1}{4}$  of the anion sites vacant<sup>1</sup> so that each In ion is six coordinated rather than eight coordinated as in fluorite itself. There are 16 formula units (i.e., 32 In atoms) per unit cell and the lattice parameter is usually quoted to be  $10.117 \text{ \AA}$ .  $\text{In}_2\text{O}_3$  is intrinsically  $n$  type due to donor defects. It was believed for many years that oxygen vacancies gave rise to shallow donor states, although recent calculations suggest that  $V_o^x$  gives an electronic state rather deep in the band gap.<sup>2</sup> This has led to the suggestion that the native defect responsible for conductivity is a singly charged interstitial complex  $(\text{In}_i^{***}\text{O}_i'')$ .<sup>3</sup>  $\text{In}_2\text{O}_3$  is also amenable to  $n$ -type doping by substitution of Sn cations onto the In sites to give indium tin oxide (ITO).<sup>4–6</sup> ITO is one of a very restricted range of materials that combines the properties of optical transparency in the visible region with a high electrical conductivity. This leads to applications in thin film solar cells and in liquid crystal and electroluminescent display devices.

Despite the significant technological importance of ITO (Refs. 4–6) many aspects of its fundamental physics have

remained controversial, including the magnitude and nature of the bulk band gap in  $\text{In}_2\text{O}_3$  itself. Despite the fact that for many years the band gap was quoted to be  $3.75 \text{ eV}$  or thereabouts, recent work has shown that there is a direct but dipole forbidden absorption onset below  $3 \text{ eV}$ .<sup>7,8</sup> Moreover, surprisingly little effort has been directed toward growth of high-quality thin films of  $\text{In}_2\text{O}_3$  or ITO. To date most work on the growth of well-ordered  $\text{In}_2\text{O}_3$  films has concentrated on deposition of  $\text{In}_2\text{O}_3$  onto alumina or yttria-stabilized zirconia single-crystal substrates by pulsed laser deposition in ultrahigh-vacuum compatible systems [i.e., “laser” molecular-beam epitaxy (MBE)],<sup>9–12</sup> although there are some reports of single-crystal growth by metal-organic chemical-vapor deposition<sup>13</sup> and by MBE using conventional indium Knudsen cells and oxygen atom plasma sources.<sup>14–17</sup> These results have prompted us to initiate a program concerned with growth of  $\text{In}_2\text{O}_3$  and ITO thin films on cubic zirconia by oxygen plasma-assisted MBE.<sup>18–22</sup>  $\text{ZrO}_2$  itself has a low symmetry monoclinic structure at room temperature but a cubic phase can be stabilized by replacement of some of the  $\text{Zr}^{4+}$  with the larger cation  $\text{Y}^{3+}$ . The charge mismatch between  $\text{Zr}^{4+}$  and  $\text{Y}^{3+}$  is compensated by the introduction of oxygen vacancies. The face-centered-cubic fluorite structure of Y-stabilized  $\text{ZrO}_2$  belongs to the space group  $Fm\bar{3}m$ . For the minimum Y concentration of around 17% required to stabilize a cubic phase, the lattice parameter can be estimated as  $a=5.142 \text{ \AA}$  from extrapolation of lattice parameters for more highly doped zirconia samples.<sup>23–25</sup> Thus at 17% Y doping the mismatch  $m$  between  $2a_s$  for the Y- $\text{ZrO}_2$  and  $a_e$  for the  $\text{In}_2\text{O}_3$  epilayer as defined by the expression<sup>26</sup>

$$m = (a_e - 2a_s)/2a_s \quad (1)$$

has a value  $m = -0.016$ , i.e., the mismatch is  $-1.6\%$ . Moreover the two structures involve very similar cation arrays but with  $\frac{1}{4}$  of the anion sites of the fluorite structure vacant in  $\text{In}_2\text{O}_3$  so that the cations are six coordinated rather than eight coordinated as in the fluorite structure. Thus Y-doped  $\text{ZrO}_2$  appears to be an ideal substrate for growth of well-ordered thin films of  $\text{In}_2\text{O}_3$ . Our work to date has shown that the growth of  $\text{In}_2\text{O}_3$  on (001)-oriented Y- $\text{ZrO}_2$  at temperatures around  $650^\circ\text{C}$  by MBE leads to continuous epitaxial films<sup>18,21</sup> but growth at higher temperatures leads the films to break up into micron-sized square islands or “dots.”<sup>19,21</sup>

In this paper we report the results of high-resolution x-ray measurements on a series of samples grown at  $900^\circ\text{C}$  over a range of deposition times. All samples were characterized by an island growth mode. Initial measurements showed that the broadening of the diffraction features was much more pronounced than expected from the dimensions of the “islands” derived from atomic force microscopy (AFM) and transmission electron microscopy (TEM). However, further experiments have shown that the x-ray scattering is sensitive to the internal structure within the dots. In addition we have found evidence for the tilting of the atomic planes in the epilayer relative to those of the substrate along the four distinct in-plane  $\langle 110 \rangle$  directions.

## II. EXPERIMENTAL PROCEDURE

Indium oxide layers with an island morphology were grown on  $1\text{ cm} \times 1\text{ cm}$  Y-stabilized  $\text{ZrO}_2(001)$  substrates with a nominal Y-doping level of 17% (as defined by the formula  $\text{Zr}_{1-x}\text{Y}_x\text{O}_{2-x/2}$  with  $x=0.17$ ) in an ultrahigh-vacuum oxide MBE system (SVT, USA) with a base pressure of  $4 \times 10^{-10}$  Torr. This incorporated liquid-nitrogen-cooled cryopanel, a hot lip indium Knudsen cell and a radio-frequency (rf) plasma oxygen atom source operated at 200 mW rf power with an oxygen background pressure of  $1.5 \times 10^{-5}$  Torr. The deposition rate for the In metal was set at  $0.01\text{ nm s}^{-1}$  using a quartz crystal monitor offset from the substrate position but the true growth rate of oxide at the substrate position was found to be  $0.04\text{ nm s}^{-1}$  as gauged by cross-sectional transmission electron microscopy. Substrates were held by gravity in a recessed Mo mounting plate and heated radiatively using a graphite filament. The sample temperature was measured by a chromel-alumel thermocouple spot welded to the cradle holding the sample mounting plate. Substrates were cleaned by exposure to the oxygen atom beam with a measured substrate temperature of  $900^\circ\text{C}$ . Island films were then grown at a substrate temperature of  $900^\circ\text{C}$  in growth runs whose duration extended between 500 and 3000 s to give nominal average film thicknesses between 200 and 1200 Å (the thickness here is defined as the thickness of indium oxide if the films had been uniform across the substrate surface). The three samples studied in detail by x-ray diffraction (XRD) involved growth times of 3000 s, 1000 s, and 500 s and are referred to as samples A, B, and C respectively. Most of the data reported here are from sample A. The thickness of the islands was roughly 2500 Å for sample A.

AFM images were recorded in a Digital Instruments Multimode scanning probe microscopy instrument with a Nanoscope IIIa controller. This was usually operated in tapping mode but images of the samples grown at  $650^\circ\text{C}$  were recorded in contact mode. The measurements employed a “J” scanner having a lateral range of approximately  $100\ \mu\text{m}$  and a vertical range of  $6\ \mu\text{m}$ . Silicon probes (Nascatec GmbH model NST NCHFR), with resonant frequencies of approximately 320 kHz were used. X, Y, and Z calibration of the AFM was accomplished by scanning a  $10\ \mu\text{m}$  pitch with a  $2000\ \text{Å}$  three-dimensional reference from Digital Instruments. Additionally some samples were studied by cross-sectional TEM, as described in detail elsewhere.<sup>21</sup>

The x-ray measurements were made with a Panalytical Materials Research Diffractometer with a focusing mirror and a four bounce Ge (111) monochromator in the incident x-ray beam. A slit before the detector was employed in most measurements. However for some high-resolution measurements, a triple bounce Ge analyzer crystal was inserted before the detector. The slit gives higher count rates but has a considerably larger angular aperture than the triple bounce analyzer. The limited angular resolution allows strong scattering to be observed as a spurious peak when only the  $2\theta$  angle is varied near a substrate Bragg reflection. This effect influences the measurements shown in Fig. 4. The sample was mounted on the sample stage with the [001] axis of the substrate perpendicular to the stage and aligned horizontally in the scattering plane to give maximum scattered intensity. The tilt angle  $\psi$  was also adjusted to ensure that [001] axis lay within the scattering plane. The sample was then aligned azimuthally with the [110] axis within the scattering plane by reference to the (113) reflection. Azimuthal  $\phi$  rotation about the [001] axis could then be used to set an [010] axis or a [110] axis in the scattering plane. Scans were performed with the wave-vector transfer ( $\Delta Q$ ) parallel (longitudinal scans) or perpendicular (transverse scans) to the [001] growth axis close the (002), (004), (204), (113), and (115) Bragg reflections of the substrate, corresponding to (004), (008), (408), (226), and (22 10) reflections of the epilayer. Throughout this paper the wave-vector transfers are given in units of inverse Ångstrom. The vertical resolution of the instrument is controlled by the vertical height of the monochromator and of the analyzer or the slit before the detector. The estimated vertical resolution of about  $0.5^\circ$  is much larger than the in-plane resolution.

## III. RESULTS

AFM images of representative areas of the three samples studied in the present work are shown in Fig. 1. In each case there is an obvious propensity for growth as square sided islands with edges aligned along  $\langle 110 \rangle$  directions of the substrate. For sample A the typical lateral island size is around  $1\ \mu\text{m}$ . A similar island size is preserved in B although the island density is lower for this sample. The sample C, which was prepared with the lowest deposition time, has smaller islands. The inset to the image for the thickest sample (A) shows a cross-sectional TEM image which reveals an island thickness of about 2500 Å. It can also be seen that the is-

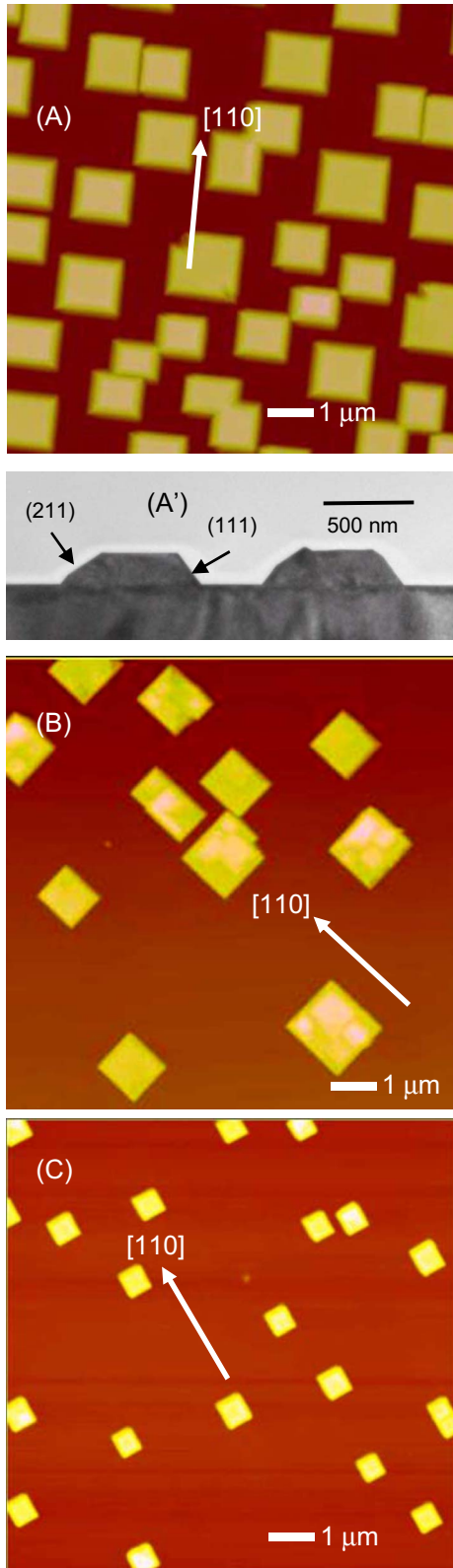


FIG. 1. (Color online)  $10\ \mu\text{m} \times 10\ \mu\text{m}$  AFM images of the three samples A, B, and C studied in the present work. The TEM micrograph shown in the panel (A') shows a cross of sample A viewed down the  $\langle 110 \rangle$  direction. The nominal average thicknesses of the films are, respectively,  $1200\ \text{\AA}$ ,  $400\ \text{\AA}$ , and  $200\ \text{\AA}$  for A, B, and C assuming uniform surface coverage, although the islands are thicker than this owing to incomplete coverage of the substrate.

lands in fact have sloping sides faces built up mostly of  $\{111\}$  facets, although  $\{211\}$  facets are also observed. AFM images show the same facet structure, although due to finite tip size effects, the side structure is not obvious in the topographic AFM images themselves and only becomes apparent in AFM “error” images.<sup>21</sup> Most of the results presented here relate to sample A, unless mentioned to the contrary.

Preliminary measurements showed that the zirconia substrates had the fluorite structure. The lattice parameter was found to be  $a = 5.1460 \pm 0.0001\ \text{\AA}$ , in good agreement with the value expected. The mosaic spread was typically less than  $0.015^\circ$ . The scattering from the indium oxide layer was both more complicated and more interesting. Figures 2(a) and 2(b) show  $\theta$ - $2\theta$  scans through the substrate (002) and (004) peaks and the associated (004) and (008) reflections of the thickest  $\text{In}_2\text{O}_3$  film presented on a linear scale. Figures 2(c) and 2(d) shows the same data but presented on a logarithmic scale in terms of the wave-vector transfer parallel to the  $[001]$  growth direction. The full widths at half maximum height of the  $\text{In}_2\text{O}_3$  peaks are  $0.016 \pm 0.001\ \text{\AA}^{-1}$  for the (004) peak and  $0.025 \pm 0.001\ \text{\AA}^{-1}$  for the (008) peak. A simple interpretation of these widths in terms of a coherent scattering thickness  $t = 2\pi/\Delta Q$  gives values of  $390\ \text{\AA}$  and  $250\ \text{\AA}$ , respectively, assuming that the islands are simple square right prismatic blocks with rectangular edges and overall  $D_{4h}$  point-group symmetry. These are very much lower than values of about  $2500\ \text{\AA}$  inferred from cross-sectional TEM. This disagreement and the difference between the results for the two different reflections are significant discrepancies and more detailed experiments were performed to understand them.

One possible source for the discrepancy is that the scattering from a truncated square pyramidal block with  $C_{4v}$  point-group symmetry is radically different from that of a square right prismatic block defined above. In order to explore this possibility we carried out model calculations of the scattering from both a square right prismatic island and a square pyramidal island with the same base size. Note that this simplified *nontruncated* pyramidal model geometry differs from the *truncated* square pyramidal geometry found experimentally. It should however produce bigger differences in scattering profiles when compared with a square right prismatic geometry and provides a simple means of exploring whether geometrical effects are important or not. The calculations were based on an idealized face-centered array of atoms, corresponding approximately to the arrangement of In atoms in  $\text{In}_2\text{O}_3$ . The pyramid had a base with  $N \times N$  atoms (where  $N$  is even) and sides with a length of  $Na/\sqrt{2}$  parallel to the  $[110]$  and  $[1\bar{1}0]$  directions, where  $a$  is the cubic lattice parameter. The edge in each successive layer had one less atom than in the preceding layer so that the sloping side facets were made up of  $\{111\}$  planes, as found experimentally. The pyramid contained  $N$  atomic layer parallel to the surface and terminated in a single atom. The calculations reported here relate to  $N=100$  and were performed by analytically summing the scattering amplitude over each basal plane and then numerically summing up these amplitudes to give the scattering amplitude for the whole pyramid. The results for the scattering intensity from a

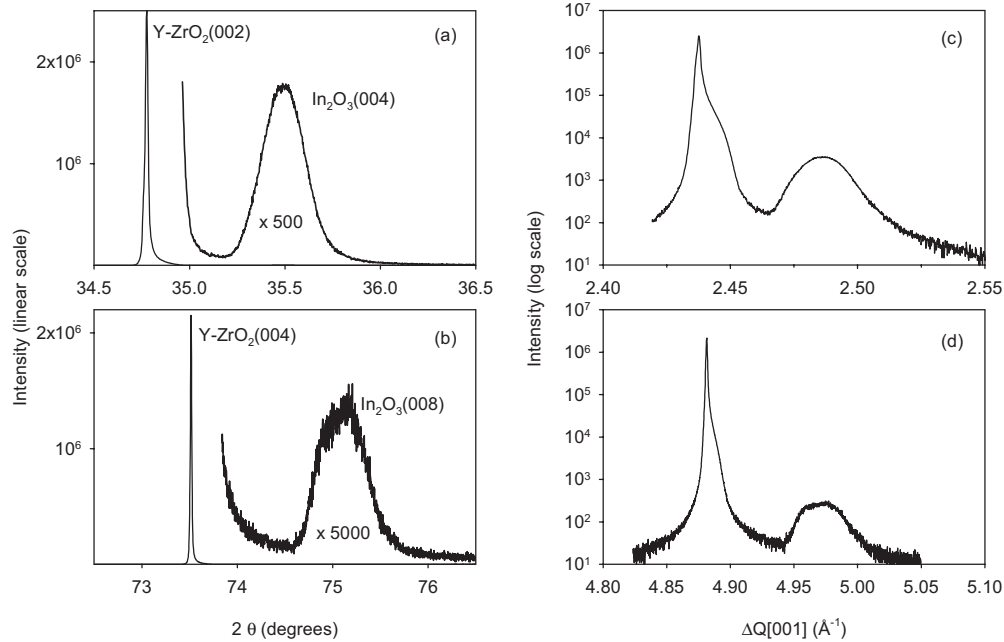


FIG. 2. X-ray scattering measured by scans of the wave-vector transfer longitudinal through the (002) and (004) Bragg reflections from the substrate and through the epilayer (004) and (008) reflections.

$C_{4v}$  square pyramid are shown in Fig. 3, where they are compared with the scattering from a  $D_{4h}$  square right prism with the same base and same height. For ease of visual comparison of the width of the peaks, the intensities have been normalized to give the same maximum intensity for both models. The scattering is shown for wave vectors near a Bragg peak and along the cubic [110], [100], and [001] directions without taking account of the form factors of the atoms, etc. Not surprisingly, the scattering for the rectangular block is narrower in wave vector than that from the pyramid and our calculations suggest that in the [100], [110], and [001] directions the pyramid gives an increase in the width over that of the rectangular block by factors of 1.31, 1.29, and 1.54, respectively. The scattering is most different for wave vectors along the [001] direction where the scattering from the square right prismatic block shows the expected oscillations associated with thickness fringes while the scattering from the pyramid steadily decreases and has a long tail. The increase in the width of the scattering for the pyramid is, however, far too small to account for the difference in the width compared with the size of the islands measured by atomic force measurements and by electron microscopy. There must therefore be other contributions to the width and the measurements reported below were performed to investigate these discrepancies.

Initially we discuss the scattering from the indium oxide near the substrate (113) reflection, corresponding to the epilayer (226) reflection. This reflection was chosen because it depends on wave-vector transfer both parallel and perpendicular to the growth direction. Transverse scans were performed with the wave-vector transfer scanned perpendicular to the growth direction for a series of different values of wave-vector transfers parallel to the growth direction. The results are shown in Fig. 4(a) which presents a map of the scattered intensity close to the (113) Bragg reflection from

the substrate. A cut through the map along the [110] direction to include the maximum in the scattered intensity is also shown in Fig. 4(b). As discussed in the experimental section, a spurious intense line arises at the bottom of the map from the use of a slit before the detector and only the broader scattering at the top of the map arises from the  $In_2O_3$  layer. An interesting feature of the results is that the maximum in the intensity is at roughly the same in-plane wave vector as for the substrate for the largest perpendicular wave-vector transfer. However, as the perpendicular wave-vector transfer decreases, the peak in the in-plane wave vector transfer moves steadily away from the value of  $1.727 \text{ \AA}^{-1}$  characteristic of the substrate. The observed change is approximately  $0.045 \pm 0.005 \text{ \AA}^{-1}$  in the plane of the film for a change of  $0.050 \pm 0.005 \text{ \AA}^{-1}$  parallel to the growth direction. The  $In_2O_3$  epilayer is placed under tensile stress by the mismatch with the substrate. The results suggest that close to the interface the indium oxide is laterally strained so that it is lattice matched to the substrate in the growth plane. This leads in turn to a contraction in  $d$  spacings parallel to the growth direction through the Poisson effect and to larger values of longitudinal wave-vector transfer than expected from the bulk lattice parameter. Away from the interface the strain is relaxed through formation of dislocations and the in-plane lattice parameter decreases while the out-of-plane lattice parameter increases, so that the resulting layer has a more nearly cubic structure. We thus find that the lattice parameters at the interface are not characteristic of a cubic material but that the  $In_2O_3$  elongates under tensile stress parallel to the surface and contracts perpendicular to it. Moreover, the scattering from the (226) epilayer reflection is very broad with a width of approximately  $0.08 \text{ \AA}^{-1}$  perpendicular to the growth direction. There are a number of possible contributions to peak width, including from finite-size effects, variations in the lattice parameter perpendicular to the growth

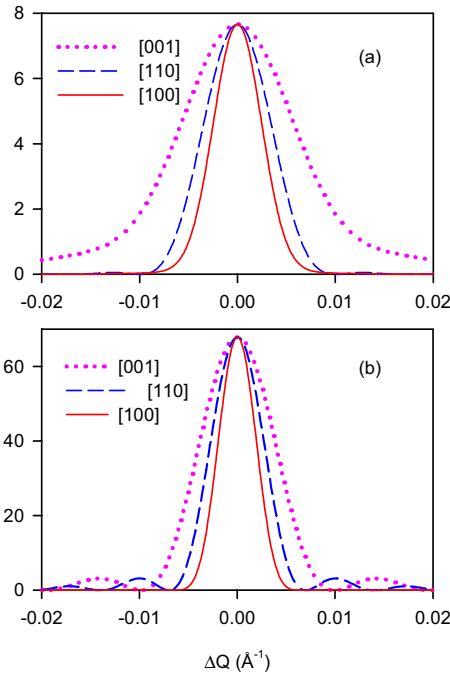


FIG. 3. (Color online) (a) The calculated scattering from a pyramid and (b) a rectangular block. The dashed line is scattering when the wave-vector transfer is along the  $[110]$  direction, one of the sides of basal plane of the pyramid, the continuous line is the scattering when the wave vector is along the  $[100]$  direction, also in the basal plane but at  $45^\circ$  to the edges of the pyramid, and the dotted line shows the scattering when the wave-vector transfer is along the  $[001]$  direction perpendicular to the basal plane. The wave vector is in units of  $2\pi/a$  and the number of lattice constants  $N$  is 100.

direction or from tilting of the atomic planes. Similar results were obtained near the (115) and (204) Bragg reflections of the substrate although these reflections were much weaker and more difficult to study in detail. Taken together the results suggest, however, that the lattice parameters of the indium oxide vary with distance from the interface and that the changing lattice constants make a substantial contribution to the x-ray linewidths in both longitudinal and transverse scans.

As mentioned previously, the width of the peaks for wave-vector transfer parallel to the growth direction is  $0.016 \pm 0.02 \text{ \AA}^{-1}$  for the (004) Bragg reflection and  $0.025 \pm 0.05 \text{ \AA}^{-1}$  for the (008) Bragg reflection. Using these two measurements we can surmise that there are two contributions to the width of the peaks. One arises from the variation in the lattice parameter resulting from strain near the interface. This is expected to vary as the wave-vector transfer squared. The other arises from the finite size of the domains that produce coherent scattering and is expected to be independent of wave-vector transfer. The latter contribution to the broadening is estimated to be  $0.013 \text{ \AA}^{-1}$  while the wave-vector-dependent contributions to the broadening are  $0.003 \text{ \AA}^{-1}$  for the (004) reflection and  $0.012 \text{ \AA}^{-1}$  for the (008) reflection. We can thus infer that the coherent scattering length is  $(2\pi/0.013) \text{ \AA}$ , which is about  $500 \text{ \AA}$ . This value is still less than the sample thickness of around  $2500 \text{ \AA}$  found by tunneling techniques and electron micros-

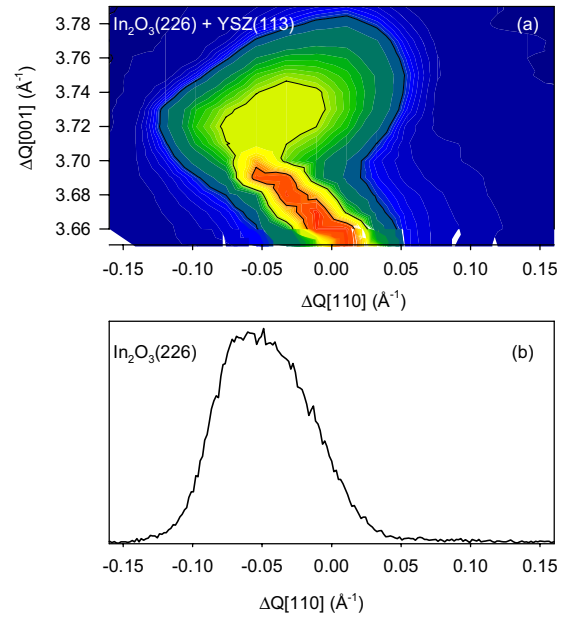


FIG. 4. (Color online) (a) A contour map of the scattering near the substrate (113) Bragg reflection presented on a logarithmic scale. The spurious diagonal streak in the lower part of the map is discussed in the text. The scattering from the  $\text{In}_2\text{O}_3$  film is the broader diffuse structure observed at larger  $\Delta Q[001]$ . The zero of the horizontal scale is defined by the position of the substrate Bragg reflection for which  $\Delta Q[110]=1.727 \text{ \AA}^{-1}$ . The lower panel shows a transverse cut through the map passing encompassing the maximum of the scattering from the  $\text{In}_2\text{O}_3$  epilayer with  $\Delta Q[001]=3.71 \text{ \AA}^{-1}$ . The cut is presented on linear scale.

copy but is significantly larger than the estimate which neglects strain.

We also made a detailed study of transverse scattering from the indium oxide close to the (002) and (004) Bragg reflections of the substrate, corresponding to the (004) and (008) reflections of the epilayer. Figure 5 shows the scattering observed when the wave-vector transfer is scanned parallel to the surface with either the  $[100]$  or  $[110]$  direction within the scattering plane. The figure includes data for the  $\text{In}_2\text{O}_3$  (004) peak in panels (a) and (b) and for the (008) peak in panels (c) and (d). The wave-vector transfer normal to the surface along the  $[001]$  direction was selected to include the overall peak maximum of the indium oxide scattering. The profiles are dependent on whether the  $[100]$  or  $[110]$  direction is in the scattering plane. The scattering observed in the  $[110]$  direction for the epilayer (004) reflection has three peaks, the central component having approximately twice the intensity of the two side peaks. The two side peaks for the (004) reflection were centered at  $\pm(0.030 \pm 0.002) \text{ \AA}^{-1}$  with a width along the  $[110]$  direction of  $0.020 \pm 0.004 \text{ \AA}^{-1}$  and the peak in the center has a similar width. The comparable scan when the  $[100]$  direction was in the scattering plane showed only two peaks. Each peak is now centered at  $\pm(0.022 \pm 0.002) \text{ \AA}^{-1}$  which is very close to a  $1/\sqrt{2}$  times the separation between the two side peaks in the  $[110]$  direction while the width had approximately the same value of  $0.020 \pm 0.005 \text{ \AA}^{-1}$ . It thus emerges that the scattering is not isotropic perpendicular to the growth direction and is consis-

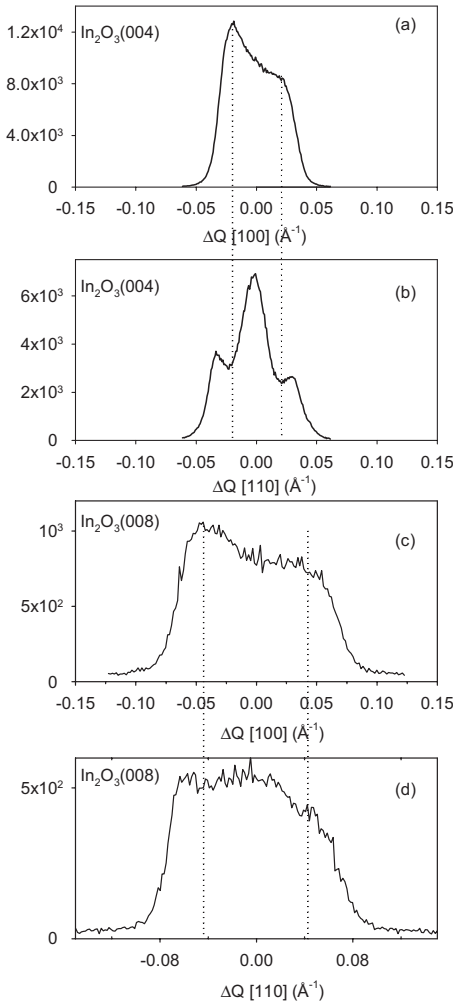


FIG. 5. [(a) and (b)] Scans of scattered intensity close to the (002) Bragg reflection of the substrate as a function of transverse wave-vector transfer. The wave-vector transfer was varied along the [100] direction in (a) and the [110] direction in (b).  $\Delta Q[001] = 2.486 \text{ \AA}^{-1}$  in both cases. [(c) and (d)] Scans of scattered intensity close to the (004) Bragg reflection of the substrate as a function of transverse wave-vector transfer. The wave-vector transfer was varied along the [100] direction in (c) and the [110] direction in (d).  $\Delta Q[001] = 4.972 \text{ \AA}^{-1}$  in both cases. The peak in the center of scan (d) is reduced in intensity as compared to figure (b) because of the finite resolution perpendicular to the scattering plane.

tent with the pattern expected if there are four maxima displaced along the four  $\langle 110 \rangle$  directions, as shown schematically in Fig. 6. The side peaks in Fig. 5(b) arise from scattering displaced in the [110] and  $[\bar{1}\bar{1}0]$  directions and the central peak from scattering displaced in the  $[1\bar{1}0]$  and  $[\bar{1}10]$  directions. The latter are observed because of divergence perpendicular to the scattering plane: the vertical divergence in these experiments is sufficient to capture intensity that is close to the scattering plane. Experiments were also performed with the analyzer crystal in place. This gives a reduced divergence perpendicular to the scattering plane and the intensity of the central peak of the epilayer (004) Bragg reflection was then about the same intensity as the side peaks. As shown in Figs. 5(c) and 5(d) the results for the

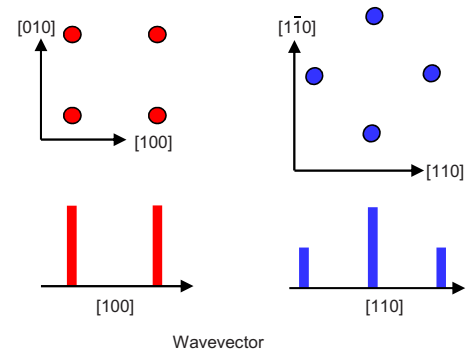


FIG. 6. (Color online) The upper panels of the figure shows a schematic representation of the positions of the scattering in the plane perpendicular to the [001] growth axis. There are four reflections displaced along the four distinct  $\langle 110 \rangle$  directions. In the experiment we observe the patterns projected into the lower panels either by scanning the wave vector along a [100] direction or along the [110] direction.

epilayer (008) peak are qualitatively very similar to the results for the epilayer (004) Bragg reflection except that peaks are found at  $\pm(0.065 \pm 0.005) \text{ \AA}^{-1}$  for the [110] direction and  $\pm(0.042 \pm 0.005) \text{ \AA}^{-1}$  in the [100] direction while the widths are approximately  $0.04 \pm 0.01 \text{ \AA}^{-1}$ . The scattering along the [110] direction now has a weaker peak in the center because the satellite peaks are further away from the scattering plane and so not all the scattering is observed in these measurements. The displacements and widths are seen to be approximately twice as large as those obtained near the (002) Bragg reflections. This shows that the structural deviation responsible for the displaced scattering from the indium oxide is not a phononlike distortion because a distortion of this sort has the same reduced wave vector in each Brillouin zone. The displaced Bragg peaks instead suggest that the indium oxide planes are tilted through a small angle along the  $\langle 110 \rangle$  directions. This tilt angle  $\psi_{[110]}$  is defined by the displacement in the transverse scan  $\Delta Q[110]$  divided by the position of the peak maximum in the longitudinal scan  $\Delta Q[001]$  because simple geometrical considerations show that  $\psi_{[110]} \approx \tan^{-1} \psi_{[110]} = \Delta Q[110] / \Delta Q[001]$ . Inserting  $\Delta Q[001] = 2.486 \text{ \AA}^{-1}$  and  $\Delta Q[110] = 0.030 \text{ \AA}^{-1}$  for the (004) Bragg peak gives  $\psi_{[110]} = 0.69^\circ$  while for the (008) Bragg peak  $\Delta Q[001] = 4.972 \text{ \AA}^{-1}$  and  $\Delta Q[110] = 0.065 \text{ \AA}^{-1}$  gives  $\psi_{[110]} = 0.75^\circ$ . We thus have an average value of  $0.72^\circ \pm 0.03^\circ$ . The width of the (008) Bragg reflection in the direction perpendicular to the growth direction is also double that observed for the (004) Bragg reflection. Hence the spread of the peak is constant in angle and corresponds to approximately  $0.45^\circ \pm 0.10^\circ$ .

Finally  $Q$  space scattering maps were constructed by scanning the wave-vector transfer parallel to the surface for a series of different values of the wave-vector transfer in the growth direction. Results of this  $Q$  space mapping for sample A are shown in Fig. 7 for both [100] and [110] directions. The tail of the substrate scattering appears as a narrow streak in the lower part of these figures. It can be seen from these maps that for the largest values of  $\Delta Q[001]$ , the scattering is weak and coincident with the peak of the substrate Bragg reflection. This is similar to the results obtained near the (113) Bragg reflection.

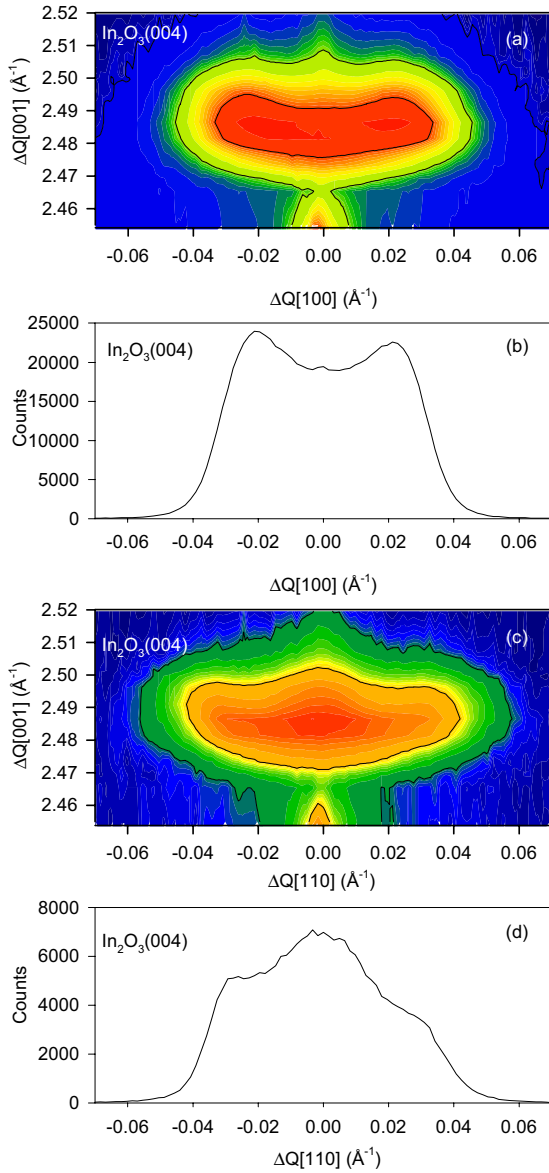


FIG. 7. (Color online) Contour maps of the variation in scattering intensity observed near the (002) Bragg reflection of the substrate for sample A. The scattering is shown for wave vectors in the plane described by the [100] and [001] directions in (a) and for the plane defined by the [110] and [001] directions in (c). The maps are presented on a logarithmic scale. Panels (b) and (d) show cuts along the [100] and [110] directions with  $\Delta Q[001]=2.486 \text{ \AA}^{-1}$  presented on a linear intensity scale.

Samples B and C gave results very similar to those for sample A and we restrict ourselves to presentation of  $Q$  space maps for these samples in Figs. 8 and 9, respectively. The scattering from the layer was approximately a factor of 10 weaker for sample B than for sample A and a factor of 50 weaker for sample C than for sample A. Sample C represents the lower limit of coverage for which it was possible to study epilayer diffraction using a laboratory based x-ray source. The maps show basically the same structure and displacements as in Fig. 8, although the separate peaks were narrower than for sample A. This is especially evident for the thinnest sample C as shown in Fig. 10. Furthermore the con-

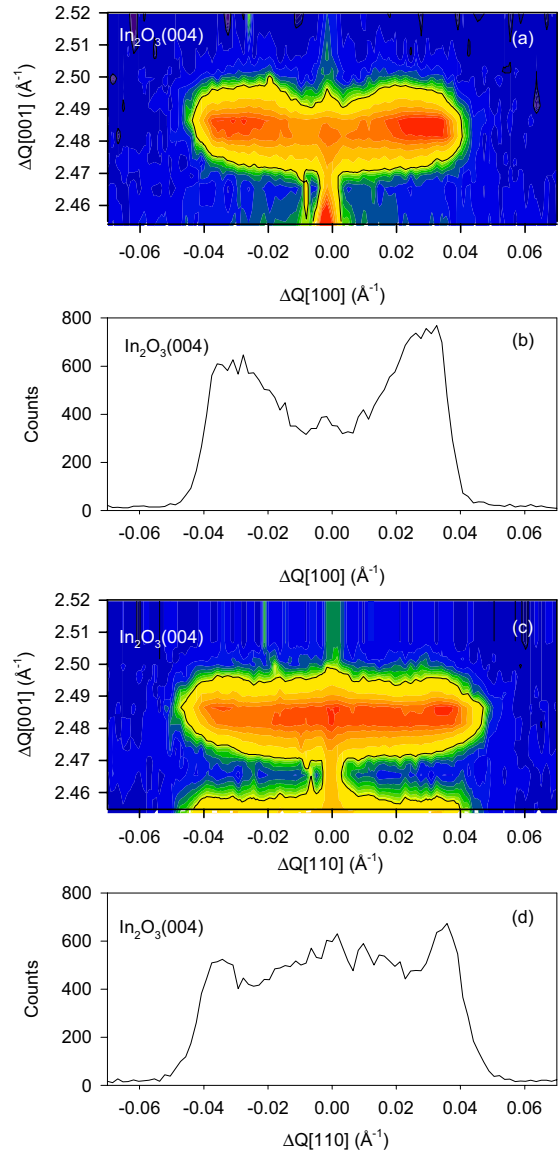


FIG. 8. (Color online) Contour map of the variation in scattering intensity observed near the (002) Bragg reflection of the substrate for sample B. The scattering is shown for wave vectors in the plane defined by the [100] and [001] directions in (a) and for the plane defined by the [110] and [001] directions in (c). The maps are presented on a logarithmic scale. Panels (b) and (d) show cuts along the [100] and [110] directions with  $\Delta Q[001]=2.486 \text{ \AA}^{-1}$  presented on a linear intensity scale.

tour maps in Figs. 9 and 10 show a sharp streak running through the center of the epilayer scattering and aligned with the Bragg reflections from the substrate in a way at least similar to that expected for a crystal truncation rod from the substrate. Possibly this is present because there are now very large regions of the surface not covered by indium oxide dots that can give this scattering while for the thicker sample crystal truncation rods are not observed because of the more closely placed islands and the much larger scattering from those islands.

The conclusion that the island epilayer is tilted relative to the substrate was confirmed by provisional high-resolution TEM (HRTEM) observations. Tilt was apparent for sections

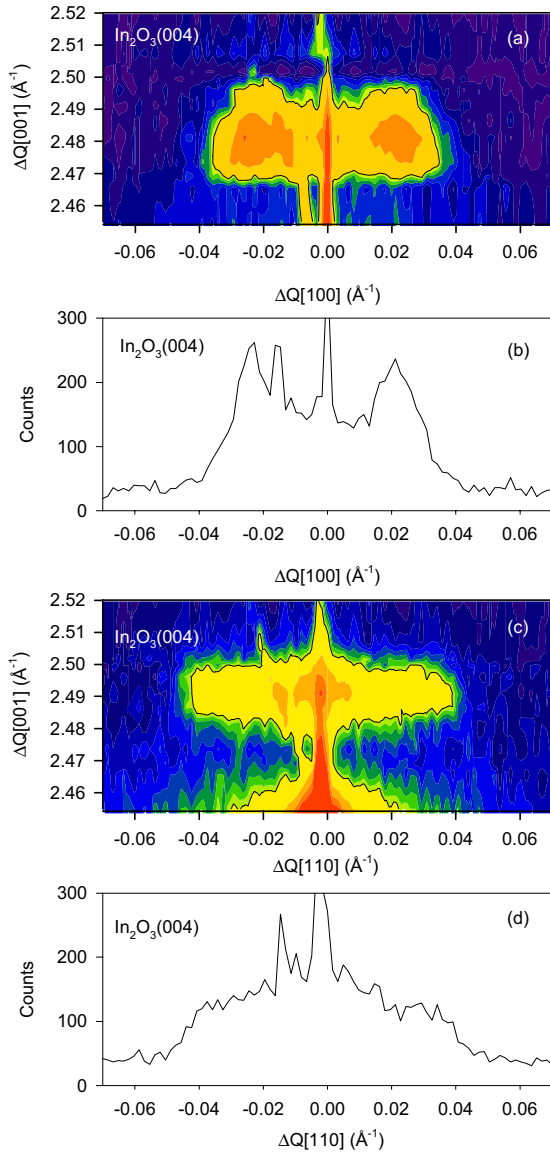


FIG. 9. (Color online) Contour map of the variation in scattering intensity observed near the (002) Bragg reflection of the substrate for sample C. The scattering is shown for wave vectors in the plane described by the [100] and [001] directions in (a) and for the plane defined by the [110] and [001] directions in (c). The maps are presented on a logarithmic scale. Panels (b) and (d) show cuts along the [100] and [110] directions with  $\Delta Q[001]=2.486 \text{ \AA}^{-1}$  presented on a linear intensity scale.

cut to allow HRTEM observations down both  $[1\bar{1}0]$  and  $[010]$  directions, as shown in Figs. 10(a) and 10(b). To emphasize the tilt and measure the tilt angles we found it convenient to change the aspect ratio of the HRTEM images by compression down the  $[001]$  axis by a factor of 5: this increases the apparent tilt angle by the same factor. The results of this procedure for the image of Fig. 10(a) are shown in panel (c), from which it is found that the local tilt angle down the  $[110]$  direction was about  $1.7^\circ$ . There were however significant variations in the local tilt angle, especially for sections viewed down the  $[010]$  direction as in Fig. 10(b). Thus the compressed version of this image shown in Fig.

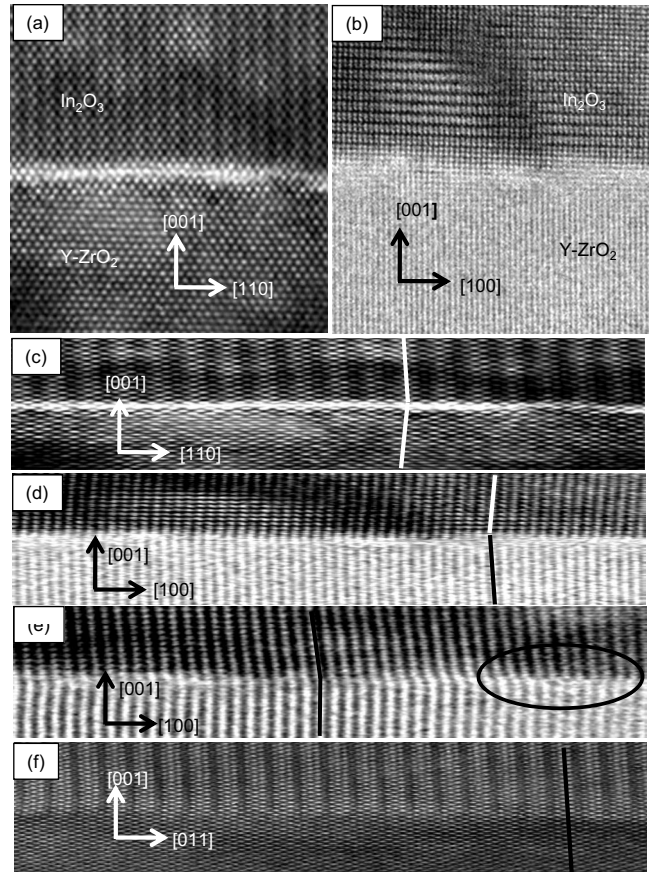


FIG. 10. (a) Cross-sectional HRTEM image of  $\text{Y-ZrO}_2/\text{In}_2\text{O}_3$  interface for sample grown under identical conditions to sample A viewed down  $[1\bar{1}0]$  direction; (b) as in (a) but for a different section viewed down  $[010]$  direction; (c) the image as in (a) but with the aspect ratio changed by a factor of 5 by compression in the  $[001]$  direction and expansion in the  $[110]$  direction in order to emphasize the tilt at the interface; (d) the image as in (b) but with the aspect ratio changed by a factor of 5 by compression in the  $[001]$  direction and expansion in the  $[100]$  direction; (e) compressed image similar to (d) but from a different island with more pronounced tilt; (f) compressed image similar to (c) viewed down  $[1\bar{1}0]$  direction for a continuous film sample grown at  $650^\circ\text{C}$ .

10(d) reveals a local tilt of  $2.0^\circ$ , whereas the tilt in another island within the same section shown in the compressed image of Fig. 10(e) is  $2.6^\circ$  in the opposite direction to that in Fig. 10(d). It is obvious that the strain state in a thin lamellar slice prepared for HRTEM (where a typical thickness will be on the order of  $300 \text{ \AA}$ ) differs from the biaxially symmetric strain state on the (001) surface of a cubic material. In addition preparation of samples for HRTEM may in itself introduce defects and dislocations, which will in turn influence the tilt angle.

As we have described elsewhere, rough but continuous  $[001]$ -oriented thin-film samples can be prepared by deposition at lower substrate temperatures of around  $650^\circ\text{C}$ .<sup>18,21</sup> These samples gave no signature of tilt in XRD or in cross-sectional HRTEM images [Fig. 10(f)]. However there is evidence of misfit dislocations very close to the interface, as seen, for example, toward the left-hand side of Fig. 10(f).

These cause the atomic rows of the epilayer in the compressed images to appear to bend in the vicinity of the dislocations. Misfit dislocations as well as tilt are found in the images from the island samples grown at high 900 °C. This is illustrated, for example, in the image shown in Fig. 10(e)—within this image there is one more epilayer atomic row than the number of substrate atomic rows and a misfit dislocation is clearly apparent in the right half of the image (highlighted by an ellipse in the figure).

#### IV. DISCUSSION

Tilting at interfaces between mismatched materials is a widespread phenomenon which has been observed in a diverse range of systems including  $\text{Si}_3\text{N}_4$  on Si,<sup>27</sup> rare-earth metals on body-centered-cubic transition metals,<sup>28</sup> and ZnSe on Ge.<sup>29</sup> Particular interest in this area has concentrated on mismatched group IV, III-V, and II-VI systems with the zincblende or diamond structures. In most of these cases the lattice parameter for the epilayer is greater than that for the substrate so that at an interface with a perfectly oriented substrate the epilayer would be placed under compressive stress. In this situation strain due to the mismatch is relieved by tilting if the epilayer is grown on a vicinally offcut substrate.<sup>30–33</sup> The direction of the offcut basically determines the direction of the tilt. The use of vicinal substrates in MBE growth of III-V materials is now widely used to improve the quality of the epilayer. The situation in the current system is somewhat different in that the lattice parameter for the epilayer is less than the (doubled) lattice parameter for the substrate so that the epilayer is placed under tensile stress along both [100] and [010] directions. A simple geometric construction then suggests that strain can be relieved by tilting with periodic introduction of tilt dislocations as shown schematically in Fig. 11(a). The step heights in these dislocations are determined by the distance between adjacent cation containing atomic planes within the epilayer. For  $\text{In}_2\text{O}_3$  this distance is  $a_e/4=2.59$  Å.

Lattice tilting as depicted in Fig. 11(a) only relieves the lattice mismatch in the tilt direction. However, in a mismatched cubic system, biaxial mismatch is clearly present along both the [100] and [010] directions. Mismatch along the in-plane direction orthogonal to the tilt direction (which is [010] for tilt along the [100] direction and  $[1\bar{1}0]$  for tilt along the [110] direction) must be accommodated by lattice straining, and this incurs a penalty in terms of the elastic strain energy. It is therefore informative to consider the relative magnitudes of the energies associated with in-plane strains along the  $\langle 100 \rangle$  and  $\langle 110 \rangle$  directions, the former being associated with the tilt along the  $\langle 100 \rangle$ , and the latter with the tilt along the  $\langle 110 \rangle$  directions, respectively. Due to the absence of large single-crystal samples, reports on the elastic properties of  $\text{In}_2\text{O}_3$  are sparse. However, an interatomic potential model for  $\text{In}_2\text{O}_3$  has recently been developed,<sup>34</sup> based on the Born model of ionic solids. This reproduces the structural, elastic, and defect properties of bixbyite, as well as a number of high-pressure phases. Using this model, the three independent elastic constants ( $c_{11}=298$  GPa,  $c_{12}=142$  GPa, and  $c_{44}=76$  GPa) were obtained from the second derivative of

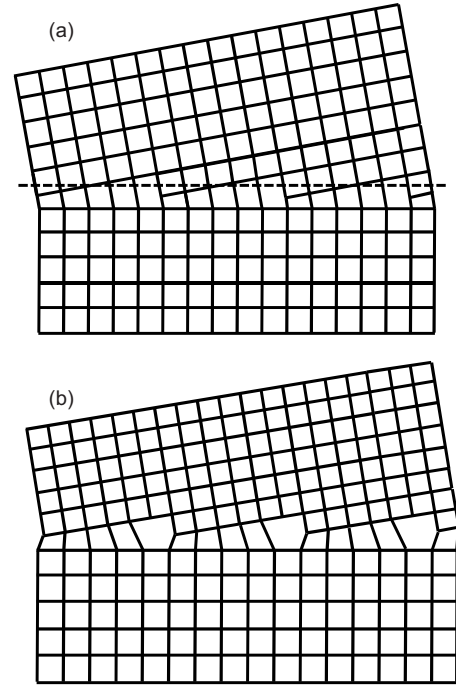


FIG. 11. (a) Schematic of tilt at the mismatched interface of two cubic materials viewed down the [010] direction where the lattice parameter of the epilayer is less than that of the substrate such that  $f=0.98$ ,  $\nu=0$ . The figure shows how registry can be maintained by tilting with a tilt angle  $\psi=10.5^\circ$  with the introduction of periodic tilt dislocations and a sawtooth variation in compressive and tensile strain at the interface. See text for definition of  $f$ ,  $\nu$ , and  $\psi$ . (b) Schematic of a more strongly mismatched interface between cubic materials as in (a) but with  $f=0.82$ . Misfit is now accommodated by introduction of both tilt dislocations and periodic misfit dislocations with  $\nu=1$  giving a tilt angle  $\psi=9.6^\circ$ .

the energy with respect to lattice strain. The energy density associated with uniaxial elastic strain in  $\langle 100 \rangle$  directions is determined by  $c_{\langle 100 \rangle}=c_{11}=298$  GPa. The corresponding stiffness constant along the  $\langle 110 \rangle$  direction is given by  $c_{\langle 110 \rangle}=(2c_{11}+2c_{12}+c_{44})/4=239$  GPa. In other words, the strain energy penalty associated with straining (and tilting) along the  $\langle 110 \rangle$  directions is approximately 20% lower than that for the  $\langle 100 \rangle$  directions. This simple reasoning shows that, in agreement with the experiment, lattice tilt along  $\langle 110 \rangle$  directions with accompanying strain in an orthogonal  $\langle 110 \rangle$  direction is favored over tilt along  $\langle 100 \rangle$  directions. There are clear analogies between the current results and those found for RbI(111) islands on basal plane mica surfaces. In this system the epilayer is also under tensile stress and tilting was found along symmetry-related azimuthal directions.<sup>35</sup>

The tilt angle suggested by the construction of Fig. 11(a) assuming that (i) the epilayer (and substrate) remain unstrained and (ii) that the number  $n$  of cation planes between tilt dislocations is such that  $n_s=n_e$  (where  $s$  refers to the substrate and  $e$  refers to the epilayer) has a value  $\psi_{[100]}$  determined by the lattice matching factor  $f=a_e/2a_s$ , where the  $a$  are lattice parameters for the substrate  $s$  and the epilayer  $e$ , respectively (remember that  $2a_s \approx a_e$ ),

$$\cos \psi_{[100]} = f. \quad (2)$$

This translates into a tilt along the  $[110]$  direction  $\psi_{[110]}$  defined by

$$\psi_{[110]} = \tan^{-1}(\sqrt{2} \times \tan \psi_{[100]}) \quad (3)$$

with  $f=0.984$ , this analysis gives a tilt angle  $\psi_{[110]}=14.5^\circ$ , which is very much bigger than observed. This suggests that the misfit is accommodated by a combination of both tilt and misfit dislocations, such that the number of In containing cation planes within a given lateral distance is greater than the number of Y/Zr-containing planes in the substrate i.e.,  $n_e > n_s$ . This situation is illustrated schematically in Fig. 11(b). The two types of dislocation may be further accompanied by elastic strain in the epilayer such that  $d_{001} < d_{100}$ , where the  $d$  are interplanar spacings. A generalized geometrical model to deal with the occurrence of both tilt and misfit dislocations (but not elastic strain) has recently been developed by Yamada *et al.*<sup>36</sup> Following these authors, we define  $\nu$  by

$$\nu = n_e - n_s. \quad (4)$$

Neglecting long-range strain in the  $\text{In}_2\text{O}_3$  other than very close to the interface we can write

$$\tan \psi_{[110]} = \frac{p(1-f^2)}{\nu + f\sqrt{\nu^2 + p(1-f^2)}}, \quad (5)$$

where  $p$  is an aspect ratio determined by the ratio of spacings between atomic layers in the  $[001]$  and  $[110]$  directions. Taking  $p=\sqrt{2}$  and  $\nu=1$  gives a tilt angle  $\psi_{[110]}=1.20^\circ$  while  $\nu=2$  gives  $\psi_{[110]}=0.63^\circ$ . The latter value is very close to that which is observed. HRTEM images such as that shown in Fig. 10(e) provide direct evidence for occurrence of the misfit dislocations required by these considerations. The model developed by Yamada *et al.* further predicts a transition between strained pseudomorphic growth and tilted growth for a critical thickness in the epilayer. As discussed above, even our thinnest samples show evidence of tilt and it has not been possible to study the ultralow coverage regime, where pseudomorphic growth is to be expected, using a laboratory-based diffractometer. In the future we will explore the transition from untilted to tilted growth using synchrotron-based diffraction techniques applied to ultrathin samples.

We were also unable in the current study to experimentally determine whether the displaced peaks postulated in Fig. 6 arise from a concerted tilt in one direction for each single island or whether there are differently tilted domains within each island. The HRTEM observations we have made so far have not revealed a change in tilt direction within a

given island but we cannot exclude this possibility. The issue is only resolvable using microdiffraction techniques and we plan further experiments using focused synchrotron radiation where it should be possible to study diffraction from single micron-sized islands. The width of the peaks in the scattering parallel to the  $[110]$  direction for the  $(004)$  reflection of the epilayer correspond to coherent domain size of about  $300 \text{ \AA}$ . The  $0.73^\circ$  average tilting of the domains implies that the periodicity for tilt dislocations parallel to the surface along the  $[110]$  direction is given by  $2.59/[\sqrt{2} \times \sin(0.73^\circ)] \text{ \AA}$ , i.e.,  $144 \text{ \AA}$  and our assumption that  $\nu=1$  or  $2$  implies that misfit dislocations are found with similar periodicity. These periodicities are in the same ball park as the coherence length and suggest that the dislocations which determine the coherence length in x-ray scattering may propagate from either tilt or misfit dislocations.

## V. CONCLUDING REMARKS

Epitaxial islands of  $\text{In}_2\text{O}_3$  grown on  $(001)$ -oriented Y-stabilized cubic  $\text{ZrO}_2$  have been studied by high-resolution x-ray diffraction in conjunction with high-resolution transmission electron microscopy and atomic force microscopy. It was found that the atomic planes in the islands are tilted relative to the planes of the substrate with tilt down the four in-plane  $\langle 110 \rangle$  directions. This tilt direction is determined by minimization of strain energy arising from lattice mismatch orthogonal to the tilt direction. To set the current results in a broader context, we note that there is no evidence of tilt for continuous thin-film samples grown of  $(001)$ -oriented substrates at lower temperatures or for films grown on  $(111)$ - or  $(110)$ -oriented substrates. The thermodynamically favored growth morphology is determined by a complex interplay between tilt and tilt dislocations, pseudomorphic strain, and misfit dislocations. We hope to develop atomistic modeling procedures which will allow us to clarify why tilt is only observed in the  $\text{In}_2\text{O}_3/\text{Y-ZrO}_2$  system for island growth on  $(001)$ -oriented substrates at elevated temperatures. We also plan to undertake synchrotron-based x-ray diffraction measurements to study ultrathin samples where strained pseudomorphic growth may be favored and to explore whether there are differently tilted domains within a single  $\text{In}_2\text{O}_3$  island.

## ACKNOWLEDGMENTS

The oxide MBE program was supported by EPSRC under Grant No. GR/S94148. R.A.C. is also grateful for financial support from the Leverhulme Foundation. We are grateful to A. Walsh for providing details of elastic constants of  $\text{In}_2\text{O}_3$  derived from atomistic simulations.

<sup>1</sup>M. Marezio, *Acta Crystallogr.* **20**, 723 (1966).

<sup>2</sup>S. Lany and A. Zunger, *Phys. Rev. Lett.* **98**, 045501 (2007).

<sup>3</sup>Y. Ohya, T. Yamamoto, and T. Ban, *J. Am. Ceram. Soc.* **91**, 240 (2008).

<sup>4</sup>C. G. Granqvist and A. Hultaker, *Thin Solid Films* **411**, 1 (2002).

<sup>5</sup>C. G. Granqvist, *Sol. Energy Mater. Sol. Cells* **91**, 1529 (2007).

<sup>6</sup>H. Hosono, *Thin Solid Films* **515**, 6000 (2007).

- <sup>7</sup>A. Walsh, J. L. F. Da Silva, S.-H. Wei, C. Körber, A. Klein, L. F. J. Piper, A. DeMasi, K. E. Smith, G. Panaccione, P. Torelli, D. J. Payne, A. Bourlange, and R. G. Egdell, *Phys. Rev. Lett.* **100**, 167402 (2008).
- <sup>8</sup>P. D. C. King, T. D. Veal, D. J. Payne, A. Bourlange, R. G. Egdell, and C. F. McConville, *Phys. Rev. Lett.* **101**, 116808 (2008).
- <sup>9</sup>M. Y. Chern, Y. C. Huang, and W. L. Xu, *Thin Solid Films* **515**, 7866 (2007).
- <sup>10</sup>H. Ohta, M. Orita, M. Hirano, H. Tanji, H. Kawazoe, and H. Hosono, *Appl. Phys. Lett.* **76**, 2740 (2000).
- <sup>11</sup>H. Ohta, M. Orita, M. Hirano, and H. Hosono, *J. Appl. Phys.* **91**, 3547 (2002).
- <sup>12</sup>T. Koida and M. Kondo, *J. Appl. Phys.* **99**, 123703 (2006).
- <sup>13</sup>Ch. Y. Wang, V. Lebedev, V. Cimalla, Th. Kups, K. Tonisch, and O. Ambacher, *Appl. Phys. Lett.* **90**, 221902 (2007).
- <sup>14</sup>N. Taga, M. Maekawa, M. Kamei, I. Yasui, and Y. Shigesato, *Jpn. J. Appl. Phys., Part 1* **37**, 6585 (1998).
- <sup>15</sup>N. Taga, M. Maekawa, Y. Shigesato, I. Yasui, M. Kamei, and T. E. Haynes, *Jpn. J. Appl. Phys., Part 1* **37**, 6524 (1998).
- <sup>16</sup>E. H. Morales, Y. B. He, M. Vinnichenko, B. Delley, and U. Diebold, *New J. Phys.* **10**, 125030 (2008).
- <sup>17</sup>E. H. Morales and U. Diebold, *Appl. Phys. Lett.* **95**, 253105 (2009).
- <sup>18</sup>A. Bourlange, D. J. Payne, R. G. Egdell, J. S. Foord, P. P. Edwards, M. O. Jones, A. Schertel, P. J. Dobson, and J. L. Hutchison, *Appl. Phys. Lett.* **92**, 092117 (2008).
- <sup>19</sup>A. Bourlange, D. J. Payne, R. M. J. Jacobs, R. G. Egdell, J. S. Foord, A. Schertel, P. J. Dobson, and J. L. Hutchison, *Chem. Mater.* **20**, 4551 (2008).
- <sup>20</sup>A. Bourlange, D. J. Payne, R. G. Palgrave, H. L. Zhang, J. S. Foord, R. G. Egdell, R. M. J. Jacobs, T. D. Veal, P. D. C. King, and C. F. McConville, *J. Appl. Phys.* **106**, 013703 (2009).
- <sup>21</sup>A. Bourlange, D. J. Payne, R. G. Palgrave, J. S. Foord, R. G. Egdell, R. M. J. Jacobs, A. Schertel, J. L. Hutchison, and P. J. Dobson, *Thin Solid Films* **517**, 4286 (2009).
- <sup>22</sup>K. H. L. Zhang, D. J. Payne, R. G. Palgrave, V. K. Lazarov, W. Chen, A. T. S. Wee, C. F. McConville, P. D. C. King, T. D. Veal, G. Panaccione, P. Lacovig, and R. G. Egdell, *Chem. Mater.* **21**, 4353 (2009).
- <sup>23</sup>H. Horiuchi, A. J. Schultz, P. C. W. Leung, and J. M. Williams, *Acta Crystallogr., Sect. B: Struct. Sci.* **40**, 367 (1984).
- <sup>24</sup>M. Morinaga, J. B. Cohen, and J. Faber, *Acta Crystallogr., Sect. A: Cryst. Phys., Diffr., Theor. Gen. Crystallogr.* **35**, 789 (1979).
- <sup>25</sup>M. Morinaga, J. B. Cohen, and J. Faber, *Acta Crystallogr., Sect. A: Cryst. Phys., Diffr., Theor. Gen. Crystallogr.* **36**, 520 (1980).
- <sup>26</sup>S. A. Chambers, *Surf. Sci. Rep.* **39**, 105 (2000).
- <sup>27</sup>B. W. Dodson, D. R. Myers, A. K. Datye, V. S. Kaushik, D. L. Kendall, and B. Martinez-Tovar, *Phys. Rev. Lett.* **61**, 2681 (1988).
- <sup>28</sup>R. Du and C. P. Flynn, *J. Phys.: Condens. Matter* **2**, 1335 (1990).
- <sup>29</sup>J. Kleiman, R. M. Park, and H. A. Mar, *J. Appl. Phys.* **64**, 1201 (1988).
- <sup>30</sup>A. Pesek, K. Hingerl, F. Riesz, and K. Lischka, *Semicond. Sci. Technol.* **6**, 705 (1991).
- <sup>31</sup>J. E. Ayers, S. K. Ghandhi, and L. J. Schowalter, *J. Cryst. Growth* **113**, 430 (1991).
- <sup>32</sup>F. Riesz, *Vacuum* **46**, 1021 (1995).
- <sup>33</sup>F. Riesz, *J. Vac. Sci. Technol. A* **14**, 425 (1996).
- <sup>34</sup>A. Walsh, C. R. A. Catlow, A. A. Sokol, and S. M. Woodley, *Chem. Mater.* **21**, 4962 (2009).
- <sup>35</sup>F. J. Lamelas, M. Xiong, and C. V. Sloane, *Phys. Rev. B* **62**, 8330 (2000).
- <sup>36</sup>A. Yamada, P. J. Fons, R. Hunger, K. Iwata, K. Matsubara, and S. Niki, *Appl. Phys. Lett.* **79**, 608 (2001).